J Mater Sci (2012) 47:360–367
DOI 10.1007/s10853-011-5805-0

Deformation-driven formation of equilibrium phases in the Cu–Ni alloys

B. B. Straumal · S. G. Protasova · A. A. Mazilkin · E. Rabkin · D. Goll · G. Schütz · B. Baretzky · R. Z. Valiev

Received: 5 June 2011 / Accepted: 18 July 2011 / Published online: 6 August 2011

Abstract The homogeneous coarse-grained (CG) Cu–Ni alloys with nickel concentrations of 9, 26, 42, and 77 wt% were produced from as-cast ingots by homogenization at 850 °C followed by quenching. The subsequent high-pressure torsion (5 torsions at 5 GPa) leads to the grain refinement (grain size about 100 nm) and to the decomposition of the supersaturated solid solution in the alloys containing 42 and 77 wt% Ni. The lattice spacing of the fine Cu-rich regions in the Cu–77 wt% Ni alloy was measured by the X-ray diffraction (XRD). They contain 28 ± 5 wt% Ni. The amount of the fine Ni-rich ferromagnetic regions in the paramagnetic Cu–42 wt% Ni alloy was estimated by comparing its magnetization with that of fully ferromagnetic Cu–77 wt% Ni alloy. According to the lever rule, these Ni-rich ferromagnetic regions contain about 88 wt% Ni. It means that the high-pressure torsion of the supersaturated Cu–Ni solid solutions produces phases which correspond to the equilibrium solubility limit at 200 ± 40 °C (Cu–77 wt% Ni alloy) and 270 ± 20 °C (Cu–42 wt% Ni alloy). To explain this phenomenon, the concept of the effective temperature proposed by Martin (Phys Rev B 30:1424, 1984) for the irradiation-driven decomposition of supersaturated solid solutions was employed. It follows from this concept that the deformation-driven decomposition of supersaturated Cu–Ni solid solutions proceeds at the mean effective temperature $T_{\text{eff}} = 235 \pm 30$ °C. The elevated effective temperature for the high-pressure torsion-driven decomposition of a supersaturated solid solution has been observed for the first time. Previously, only the T_{eff} equal to the room temperature was observed in the Al–Zn alloys.

B. B. Straumal · S. G. Protasova · A. A. Mazilkin · B. Baretzky
Institut für Nanotechnologie, Karlsruher Institut für Technologie (KIT), Hermann-von-Helmholtz-Platz 1,
76344 Eggenstein-Leopoldshafen, Germany

B. B. Straumal (✉) · S. G. Protasova · A. A. Mazilkin
Institute of Solid State Physics, Russian Academy of Sciences, Chernogolovka, Moscow district, Russia 142432
e-mail: straumal@issp.ac.ru; straumal@mf.mpg.de

E. Rabkin
Department of Materials Engineering, TECHNION—Israel Institute of Technology, 32000 Haifa, Israel

D. Goll · G. Schütz
Max-Planck-Institut für Intelligente Systeme (formerly MPI for Metals Research), Heisenbergstrasse 3,
70569 Stuttgart, Germany

D. Goll
Hochschule Aalen, Beethovenstraße 1, 73430 Aalen, Germany

R. Z. Valiev
Ufa State Aviation Technical University, 12 K. Marx str.,
450000 Ufa, Russia

Introduction

High external driving forces for atom movement can significantly change the conditions for the atomic diffusion and phase equilibria in solids [1–5]. The term "driven systems" is frequently used to describe the behavior of materials under strong irradiation, severe plastic deformation, and collisions with projectiles etc. [6–14]. For example, the formation of supersaturated solid solutions in immiscible systems or, conversely, the dissolution of nominally thermodynamically stable precipitates was often observed in alloys under strong neutron irradiation [7, 8, 10, 13]. The interaction with intensive neutron fluxes is typical for the structural materials used in the nuclear reactors. The neutron–atom collisions during neutron

irradiation ensure the accelerated "ballistic" diffusion even at the temperatures at which the atoms are kinetically "frozen" without irradiation [15]. To describe this phenomenon, the concept of effective temperature was introduced by Martin [6]. This concept works well for the materials under neutron irradiation, where the "ballistic" (i.e. determined by atom displacements caused by neutron impact) and intrinsic (i.e. mediated by point defects) chemical interdiffusion coefficients have the same order of magnitude [16–18].

In the recent years, the concept of driven systems has been extended to cover the materials undergoing severe plastic deformation (SPD) [7–14]. The examples of various SPD processes include severe drawing of wires, multiple forging or rolling with intermediate folding of sheets, deformation of the upper layer of steel rails, high-pressure torsion (HPT), equal channel angular pressing (ECAP), twist extrusion, and high energy ball milling [19–22]. Most of these SPD modes introduce severe multiple shear in the material. In the spirit of Martin's model, this shear induces ballistic intermixing of the alloy components and competes with point defects mediated diffusion, accelerated due to increased defect generation during deformation. The outcome of this competition depends on dominating deformation mechanism and could be quite different in different systems. In particular, it has been observed recently that HPT causes dissolution or decomposition of the nonequilibrium phases (like supersaturated solid solution in the Al–Zn alloys or retained austenite and Hägg carbide in the Fe–C alloys), leaving the phases which are thermodynamically stable at the global temperature and pressure of the process (i.e. almost pure Al and Zn in the Al–Zn alloys [23, 24] or ferrite and cementite in the Fe–C system [25, 26]). On the other hand, HPT of NiTi, Nd–Fe–B or Nb–Zr–Y alloys leads to the amorphization of the crystalline samples [27–30]. Therefore, the effective temperature in the driven systems processed by SPD could be both equal or higher than the global temperature of the treatment. Since both the ballistic atomic movements induced by shear deformation and the entropy-driven diffusion mediated by point defects strongly depend on the material parameters (i.e. slip geometry, stacking fault energy, vacancy formation energy, and elastic moduli, etc.), no universal criterion capable of predicting the effective temperature for particular material has been suggested so far. The goal of this work is to investigate the phase stability of homogenized equilibrium and supersaturated solid solutions in the Cu–Ni system after HPT.

Experimental

The samples of Cu–Ni alloys in the form of cylindrical 12 mm-diameter ingots (with nickel concentrations of 9, 26, 42, and 77 wt%) were prepared from high-purity 5N8 Cu and 4N Ni by the vacuum induction melting. The ingots were sealed into evacuated silica ampoules with a residual pressure of approximately 4×10^{-4} Pa and homogenized in the one-phase (Cu, Ni) area of the Cu–Ni phase diagram [31] (Fig. 1) at 850 °C during 500 h. The 0.7-mm thick disks of these alloys obtained after sawing, grinding, and chemical etching were subjected to high-pressure torsion (HPT) at room temperature under the pressure of 5 GPa in a Bridgman anvil type unit (5 torsions, duration of process about 300 s) [21]. For the metallographic analysis after quenching, the homogenized specimens were embedded in resin and then mechanically ground and polished, using 1 μm diamond paste in the last polishing step, and etched for 5–10 s with a 5 wt% HNO_3 solution in ethyl alcohol. X-ray diffraction (XRD) data were obtained on a Siemens diffractometer (Fe K_α radiation). The line profile fitting procedure for the calculation of the lattice spacing was executed by the approximation with the Voigt function in the ORIGIN software package. Possible error due to the sample misalignment was excluded by recording the spectra of an Al powder reference sample. Lattice parameters were determined by the Nelson–Riley technique. Transmission electron microscopy (TEM) investigations of as-cast coarse-grained (CG) and fine-grained HPT-samples have been carried out in a JEM–4000FX microscope at an accelerating voltage of 400 kV. The magnetic properties were measured on a superconducting quantum interference device SQUID (Quantum Design MPMS-7 and MPMS-XL). The magnetic field was applied parallel to the sample plane (in-plane).

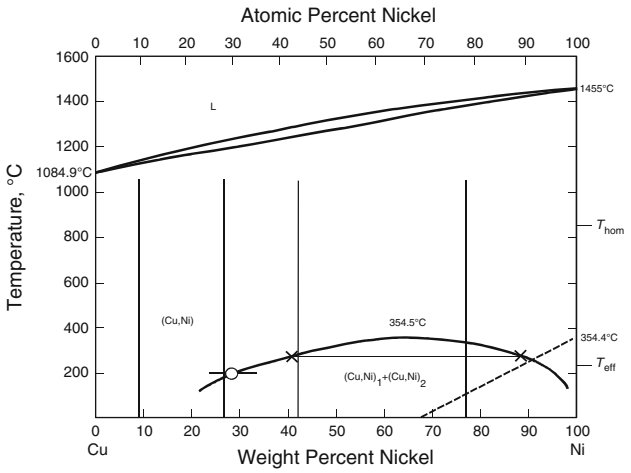

Fig. 1 Cu–Ni bulk phase diagram [31]. The compositions of studied alloys are marked by *thin vertical lines*. $T_{hom} = 850$ °C is the homogenization temperature. $T_{eff} = 235 \pm 20$ °C is the effective temperature. *Open circle* shows the composition of the Cu-rich regions in the Cu–77 wt% Ni alloy (obtained by XRD measurements). *Crosses* show the ends of the tie-line for the Cu-rich regions and Ni-rich matrix for the Cu–42 wt% Ni alloy (obtained by magnetic measurements)

Results and discussion

In Fig. 1, the Cu–Ni bulk phase diagram [31] is shown. Thick solid lines denote bulk phase equilibrium. The composition of studied alloys is marked by the thin vertical lines. The light microscopy and TEM studies demonstrated that all homogenized as-cast Cu–Ni alloys exhibit large equiaxial grains and uniform grain size of about 100 μm. They consisted solely of homogeneous supersaturated (Cu–Ni) solid solution. The XRD does not reveal any decomposition of the solid solution. According to the Cu–Ni phase diagram (Fig. 1), the solid solution is supersaturated at room temperature in all alloys with the exception of Cu–9 wt% Ni.

After deformation the grain size decreased drastically to about 100 nm (see Fig. 2). The TEM diffraction pattern revealed only a single phase—namely supersaturated solid solution. Only in Cu–77 wt% Ni some indications of decomposition can be observed by electron diffraction in TEM. X-ray diffraction of Cu–9 wt% Ni, Cu–26 wt% Ni, and Cu–42 wt% Ni alloys after HPT-treatment revealed also only a single phase, namely the Cu–Ni solid solution (see Fig. 3a). However, XRD pattern of Cu–77 wt%Ni alloy after HPT-treatment exhibits clearly visible "shoulder" on the left side of main peaks (Fig. 3b). These "shoulders" indicate the onset of decomposition of the supersaturated (Cu, Ni) solid solution into Cu-rich and Ni-rich phases, both having a face-centered cubic (fcc) lattice.

Figure 4 shows the dependence of the lattice parameter *a* calculated from XRD data on the Ni content. The lattice parameter *a* measured from the major peaks almost linearly decreases with increasing Ni concentration and coincides well with the data known from the literature (dashed lines [32, 33]). The second point for the Cu–77 wt%Ni alloy after HPT-treatment corresponds to the minor phase (Cu-rich regions). The location of the secondary peak in Fig. 3b

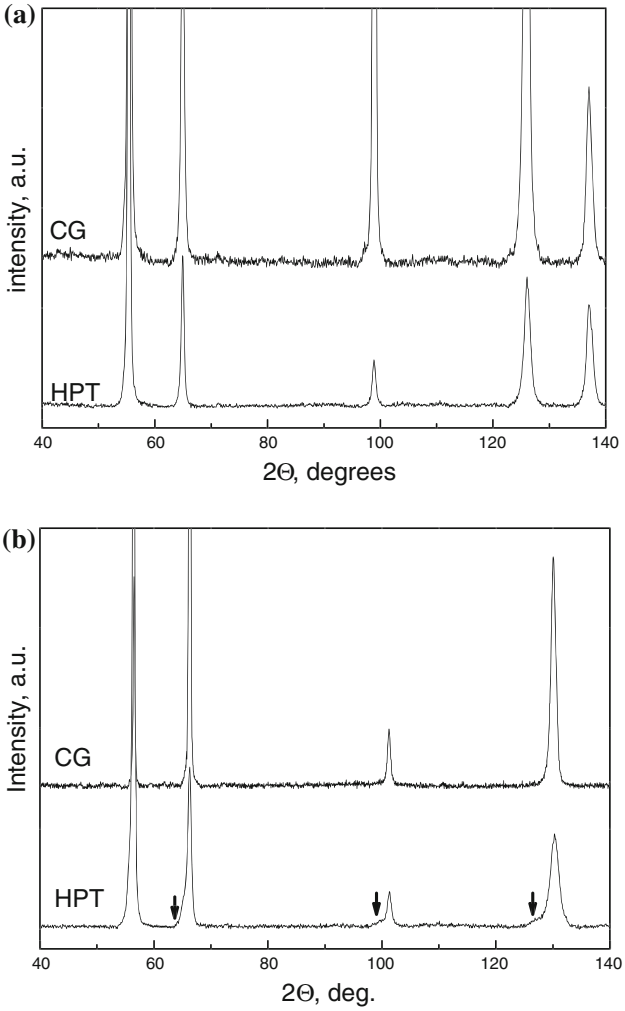

Fig. 3 **a** XRD pattern of Cu–9 wt%Ni alloy in the CG homogenized state and after HPT-treatment. Only solid-solution diffraction peaks are visible. **b** XRD pattern of Cu–77 wt% Ni alloy in a CG state and after HPT-treatment. The additional shoulder on the *left side* of the main diffraction peaks of the supersaturated solid solution in the HPT-processed alloy is visible (*marked by arrows*)

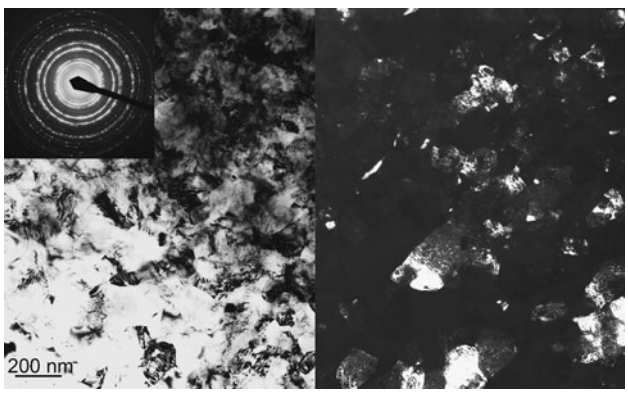

Fig. 2 TEM micrograph of the Cu–77 wt% Ni alloy after HPT (*bright field* left, and *dark field* right). Diffraction pattern reveals only a single phase

corresponds to Cu–28 ± 5 wt% Ni alloy. This means that HPT indeed leads to the decomposition of the supersaturated (Cu, Ni) solid solution in the Cu–77 wt% Ni alloy.

The measurements of the magnetization curves for the homogenized CG alloys show that the Cu–9 wt% Ni alloy reveals the diamagnetic behavior (Fig. 5a), the diamagnetism in the Cu–26 wt% Ni is weaker than in the Cu–9 wt% Ni alloy (Fig. 5c), the Cu–42 wt% Ni alloy becomes paramagnetic (Fig. 5e), and the Cu–77 wt% Ni alloy is purely ferromagnetic (Fig. 5g). This behavior is quite classic and reflects the fact that the Cu–Ni alloys quenched after homogenization contain the homogenous fcc solid solution. The continuous increase of the content of "magnetic" Ni atoms consecutively switches the magnetic behavior from dia-, through para- to ferromagnetic.

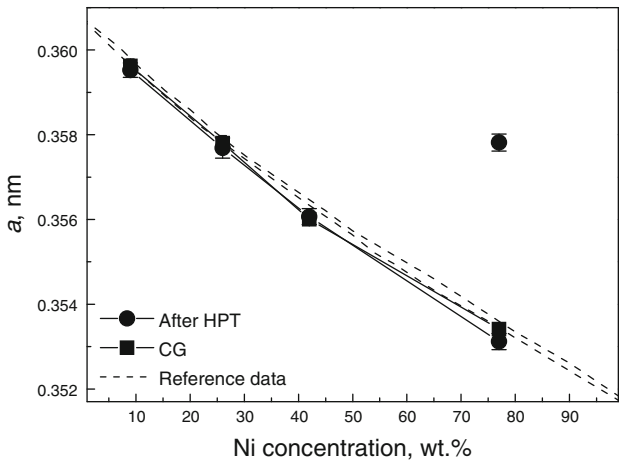

Fig. 4 Lattice spacing in the investigated Cu–Ni alloys. *Squares* mark the data for the homogenized CG alloys before HPT. *Circles* mark the data for the alloys after HPT. *Dashed lines* show the reference data from [32, 33]

This behavior corresponds well to the known phase diagram (Fig. 1).

After HPT, the Cu–9 wt% Ni (Fig. 5b) and Cu–26 wt% Ni (Fig. 5d) alloys remain diamagnetic with the same very small amount of ferromagnetic impurities. No sign of the new Ni-rich regions are visible. The Cu–77 wt% Ni alloy remains purely ferromagnetic (Fig. 5h). There is no observable difference between saturation magnetization of this alloy before and after HPT (Figs. 5g, h, 6). It means that the amount of the diamagnetic Cu-rich phase is very small and the Cu–77 wt% Ni alloy did not fully decompose according to the tie-line at 200 °C (Fig. 1). This fact corresponds well with low intensity of XRD peaks for the Cu-rich precipitates (Fig. 3b) and with TEM observations. The Cu–42 wt% Ni alloy remains paramagnetic; however, its magnetization curve exhibits a certain amount of ferromagnetic phase (Fig. 5f). The ferromagnetic component was extracted from dependences shown in Fig. 5 and the saturation magnetization was calculated. Figure 6 shows the dependence of this extracted saturation magnetization on the Ni content. It can be seen that in the Cu–9 wt% Ni (Fig. 5a, b) and Cu–26 wt% Ni (Fig. 5c, d) alloys, the ferromagnetic component is almost the same and very weak. It corresponds to a very low amount of ferromagnetic impurities. The magnetization of the Cu–77 wt% Ni alloy also remains unchanged after HPT because both alloys were ferromagnetic before and after HPT-treatment. The Cu-enriched regions observed in the HPT-processed Cu–77 wt% Ni alloy by XRD are diamagnetic (Fig. 5c, d). However, the fraction of these diamagnetic regions in the HPT-treated Cu–77 wt% Ni alloys is very small (Fig. 5b), and their input into decrease of the saturation magnetization is negligible in comparison with high signal from the major ferromagnetic phase (Fig. 5g, h).

The behavior of the Cu–42 wt% Ni alloy is more interesting. In the homogenized and quenched Cu–42 wt% Ni alloy (Fig. 5e), the ferromagnetic component was as weak as in the Cu–9 wt% Ni (Fig. 5a) and Cu–26 wt% Ni (Fig. 5c) alloys. However, HPT leads to certain decomposition of the supersaturated solid solution, and small amount of the Ni-rich ferromagnetic phase can be detected in the alloy. Generally, magnetic measurements allow observing the amounts of ferromagnetic phase in the para- or diamagnetic matrix which are much lower than the detection limit of XRD. Electron diffraction is even less sensitive to the small amounts of a second phase. If we suppose that the magnetization of the ferromagnetic regions in the Cu–42 wt% Ni alloy is the same as that of the fully ferromagnetic Cu–77 wt% Ni alloy (about 25 emu/g, see Fig. 6), we can estimate that the weight fraction of these regions is about 0.06 wt%. Based on this data and the lever rule one can construct the respective tie-line for the Cu–42 wt% Ni alloy (shown by crosses in Fig. 1). The position of this tie-line allows estimating the composition of the Ni-rich regions as Cu–88 wt% Ni.

Assuming that the composition of the Cu- and Ni-enriched region formed during HPT processing from the supersaturated Cu–Ni matrix corresponds to the solubility limit at the effective temperature of the HPT-treatment, T_{eff}, yields 270 ± 20 and 200 ± 40 °C for the Cu–42 wt% Ni and Cu–77 wt% Ni alloys, respectively (see Fig. 1). Previously, we observed that the HPT of supersaturated solid solution leads to its decomposition with the formation of phases which are at equilibrium at room temperature [23, 24, 34]. A possible explanation of these facts is offered by the "effective temperature" concept firstly proposed by Martin [6]. According to this model, the steady-state phase composition of the binary alloy undergoing forced mixing (due to irradiation or SPD) can be obtained from the corresponding equilibrium phase diagram, but at the "effective" temperature which is higher than global, physical temperature (even though the forced mixing does not increase the latter). The amplitude of the difference between physical and "effective" temperature is determined by the parameters of forced mixing (i.e. by the irradiation doze during irradiation treatment). If the "effective" temperature during our HPT-treatments was around 235 °C, this would explain relative stability of Cu–Ni alloys containing 9 and 26 wt% of Ni, since these compositions are located in the single phase area of the phase diagram at 235 °C (see Fig. 1).

Recently, it has been observed that nanostructured materials can exhibit the enhanced equilibrium solute solubility [35, 36]. However, this effect is significant only for the extremely fine-grained polycrystals (with a grain size below 15–20 nm) and for the multilayer GB segregation. Cu and Ni are fully miscible above 354.5 °C (Fig. 1). The

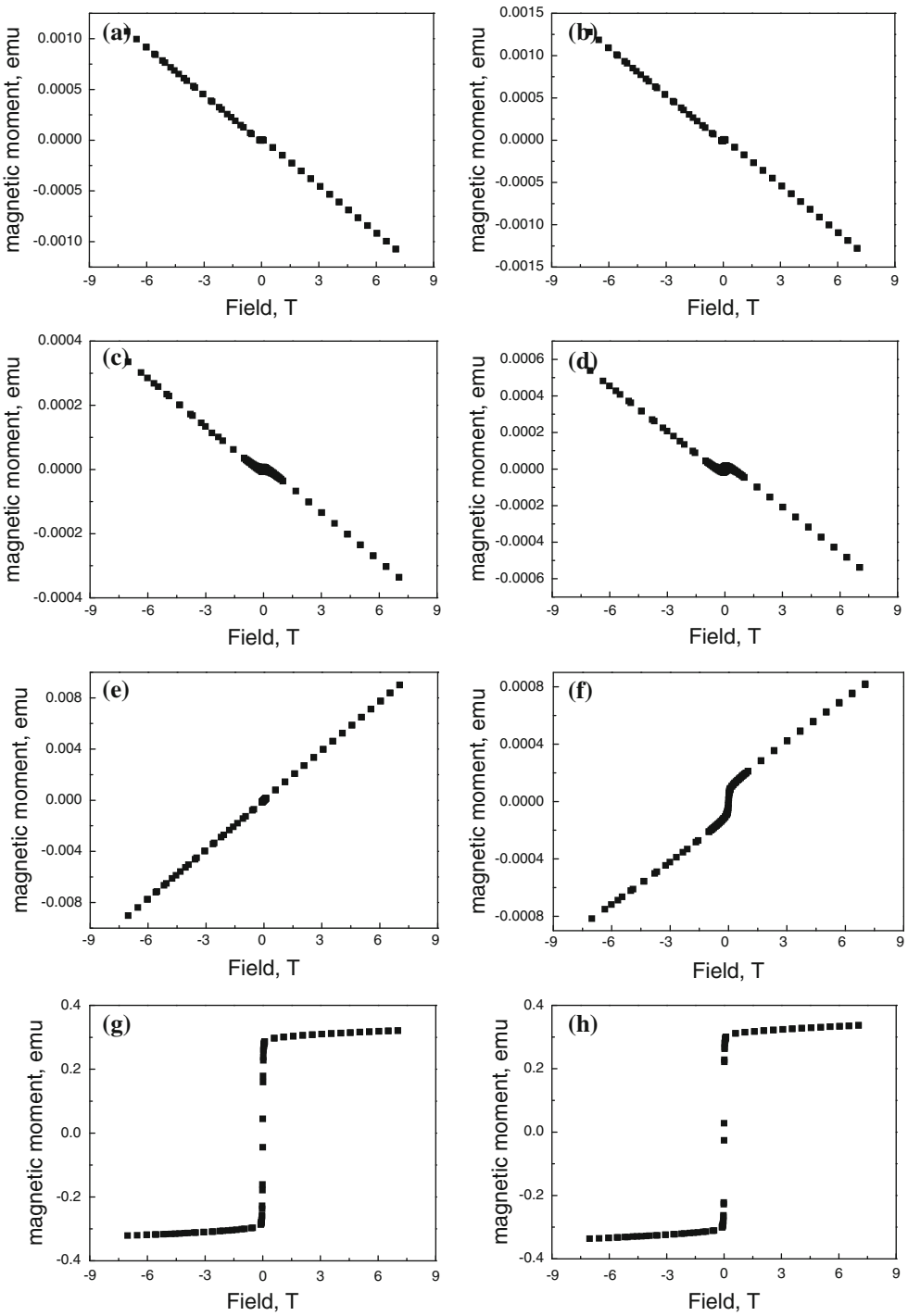

Fig. 5 Magnetization curves for **a** Cu–9 wt% Ni, **c** Cu–26 wt% Ni, **e** Cu–42 wt% Ni, and **g** Cu–77 wt% Ni as-cast alloys and **b** Cu–9 wt% Ni, **d** Cu–26 wt% Ni, **f** Cu–42 wt% Ni, and **h** Cu–77 wt% Ni alloys after HPT

strong GB segregation is very unlikely in such systems and it was never observed in the Cu–Ni alloys. In the case of monolayer GB segregation, the 100% enrichment of a 0.5 nm thick GBs between 100 nm grains would shift the solubility limit only for about 0.5%. This small effect cannot explain the difference between the observed composition of phases after HPT and solubility of Cu in Ni or Ni in Cu at the HPT temperature.

Thus, we observed that $T_{\text{eff}} = 270 \pm 20$ and 200 ± 40 °C for the Cu–42 wt% Ni and Cu–77 wt% Ni alloys, respectively. The elevated effective temperature for the HPT-driven decomposition of a supersaturated solid solution has been observed in this work for the first time. Previously, only the T_{eff} equal to the room temperature was observed in the Al–Zn alloys [23, 24, 34]. It cannot be excluded that the observed difference of the effective temperature in different

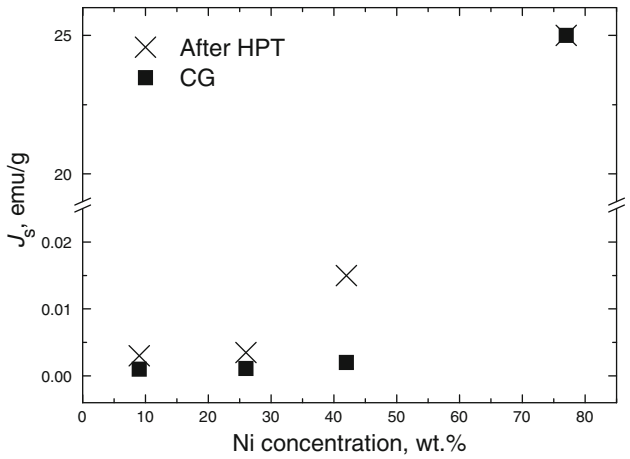

Fig. 6 Dependence of the saturation magnetization of the ferromagnetic component (extracted from the magnetization curves in Fig. 5) on the Ni content

Cu–Ni alloys is not an artifact due to the difference in measurement methods (XRD and magnetic measurements), and T_{eff} indeed depends on alloy composition.

According to Martin's theory of driven systems [6], the effective temperature of the alloy under irradiation or severe plastic shear can be written down in the following form:

$$T_{\text{eff}} = T(1 + \Delta); \quad \Delta = \frac{D_{\text{B}}}{D} \tag{1}$$

where T is the "physical" temperature of the alloy, D is the chemical interdiffusion coefficient in the alloy at the temperature T (possibly increased by the nonequilibrium concentration of point defects), and D_{B} is the "ballistic" interdiffusion coefficient describing forced mixing under the action of external driving force [6]. Let us first estimate the value of D. Assuming that the average diffusion length, L, in this case coincides with the average grain size (100 nm), we can estimate the value of D which ensures the decomposition of a supersaturated solid solution employing an approximate relationship $L \approx (Dt)^{0.5}$ ($t = 300$ s being the HPT-treatment duration). This yields $D = 3 \times 10^{-17}$ m^2/s. It is also well possible that the GB, rather than bulk interdiffusion is a process controlling the decomposition or precipitation kinetics. However, there are too many unknown variables (i.e. the migration rate of GBs during HPT processing, average size, and spacing of precipitates, etc.) which make difficult even a rough estimate of the GB diffusion coefficient needed to ensure precipitation or decomposition at room temperature.

In our opinion, it is unlikely that the bulk interdiffusion is responsible for decomposition during the HPT processing. Indeed, the range of bulk chemical interdiffusion coefficients in the Cu–Ni alloys at room temperature can be estimated by impurity diffusion coefficients of Ni in Cu, $D_{\text{Cu}}^{\text{Ni}}$ and Cu in Ni, $D_{\text{Ni}}^{\text{Cu}}$. Extrapolating the literature data to the room temperature (27 °C) yields $D_{\text{Cu}}^{\text{Ni}} = 4.8 \times 10^{-44}$ m^2/s and $D_{\text{Ni}}^{\text{Cu}} = 2.3 \times 10^{-49}$ m^2/s [38]. These diffusivities can be significantly increased by the nonequilibrium excess vacancies produced during HPT. Assuming that the highest vacancy concentration that a solid can sustain corresponds to the equilibrium vacancy concentration at the melting temperature, and with literature values of vacancy formation enthalpies of 1.28 and 1.88 eV for Cu and Ni, respectively [39], we estimate the maximal room temperature diffusivities as $D_{\text{Cu}}^{\text{Ni}} = 3 \times 10^{-27}$ m^2/s and $D_{\text{Ni}}^{\text{Cu}} = 3 \times 10^{-23}$ m^2/s. These values are still 6–10 orders of magnitude lower than our estimate $D = 3 \times 10^{-17}$ m^2/s. The external pressure can additionally slow down the diffusion [40, 41]. At the same time, extrapolating the diffusion coefficients along the "ultrafast" GBs measured recently in the pure Ni [42] and Cu–Zr alloy [43] processed by equal channel angular pressing (ECAP) yields the room temperature GB diffusivities in the range of 3×10^{-20} m^2/s. This is closer to our estimate of $D = 3 \times 10^{-17}$ m^2/s, with the remaining difference of three orders of magnitude being possibly associated with the uncertainties in determining D, the differences between the ECAP and HPT processes, and with the fact that diffusion measurements in [42, 44] were performed after the ECAP process, so that a significant part of nonequilibrium defects had a time to annihilate. In conclusion, simple estimates presented above lend credibility to the hypothesis that the GB, rather than bulk interdiffusion controls the decomposition process in the Cu–42 wt% Ni and Cu–77 wt% Ni alloys.

Substituting in Eq. 1, our estimate $D = 3 \times 10^{-17}$ m^2/s yields $D_{\text{B}} = 2.4 \times 10^{-17}$ m^2/s for the "ballistic" interdiffusion coefficient. The physical mechanism of the intermixing induced by plastic shear is a roughening of the bi-material interface [44]. This roughening is kinematic in nature (i.e. controlled mainly by slip geometry), and is a weak function of the other material constants. This provides an explanation why in the Al–Zn alloys the effective temperature of HPT was close to the room temperature. Indeed, the chemical interdiffusion coefficient in Al–Zn is many orders of magnitude higher than that in Cu–Ni at the same temperature, due to the higher melting point of the latter. For example, the impurity diffusion coefficient of Zn in Al, extrapolated to the room temperature from the data of high temperature measurements is 4.7×10^{-26} m^2/s, which is by 18 orders of magnitude larger than $D_{\text{Cu}}^{\text{Ni}}$ [38]. Taking into account the nonequilibrium defects produced during HPT decreases this enormous gap, but still the difference of several orders of magnitude remains. Assuming that D_{B} in the Al–Zn system is comparable with that for the Cu–Ni system, this means that $\Delta << 1$ in

Al–Zn and, according to Eq. 1, $T_{eff} \approx T$, as observed in the experiments [23, 24, 34].

Conclusions

From the results of the present study, the following conclusions can be drawn:

1. Similar to many other alloys, the HPT of CG homogeneous Cu–Ni alloys leads to the strong grain refinement down to the average grain size of about 100 nm. This means that the deformation drives a system from the more thermodynamically stable CG state toward the less stable nano-grained one.
2. Similar to the case of Al–Zn alloys, the HPT of the Cu–42 wt% Ni and Cu–77 wt% Ni supersaturated solid solutions leads to its decomposition in Ni-rich and Cu-rich phases, respectively. This means that severe plastic deformation drives a system from the less thermodynamically stable supersaturated state toward the more stable two-phase state. Thus, the SPD leads simultaneously to the formation of the less stable grain structure and more stable phase structure.
3. In the case of Al–Zn alloys [23, 24, 34], the phases formed after HPT-treatment of the supersaturated Al(Zn) solid solution exhibit the compositions corresponding to the room temperature equilibrium (almost pure Zn and Al). In the case of Cu–Ni alloys, the composition of the grains formed after the HPT-treatment corresponds to the solubility limit at elevated temperatures ($T_{eff} = 200 \pm 40$ °C in the Cu–77 wt% Ni alloy and $T_{eff} = 270 \pm 20$ °C in the Cu–42 wt% Ni alloy).
4. The estimates of the diffusion rate needed for the decomposition of supersaturated Cu–77 wt% Ni and Cu–42 wt% Ni solid solutions demonstrate that it can be ensured by the anomalously fast diffusion along the nonequilibrium GBs formed during HPT.
5. The "ballistic" chemical interdiffusion coefficient in the Cu–Ni system describing the forced mixing of the components during HPT induced by high shear strain has been estimated as $D_B = 2.4 \times 10^{-17}$ m^2/s. The concept of effective temperature proposed by Martin [6] was employed for describing the differences in decomposition behavior of the Al–Zn and Cu–Ni systems. The proximity of the effective temperature of the Al–Zn alloys to the room temperature is explained by the higher (if compared with Cu–Ni alloys) atomic diffusivities at the room temperature.

Acknowledgements The investigations were partly supported by Russian Foundation for Basic Research (contracts 09-03-92481, 09-08-90406 and 11-08-90439) and Israel Ministry of Science (contract 3-5790). Authors cordially thank Prof. A.M. Gusak for stimulating discussions.

References

1. Kunimine T, Aragaki T, Fujii T et al (2011) J Mater Sci 46:4302. doi:10.1007/s10853-010-5243-4
2. Rebhi A, Makhlouf T, Champion Y et al (2011) J Mater Sci 46:2185. doi:10.1007/s10853-010-5056-5
3. Wang CT, Gao N, Wood RJK et al (2011) J Mater Sci 46:123. doi:10.1007/s10853-010-4862-0
4. Kawasaki M, Mendes AD, Sordi VL et al (2011) J Mater Sci 46:155. doi:10.1007/s10853-010-4889-2
5. Zrnik J, Pippan R, Scheriau S et al (2010) J Mater Sci 45:4822. doi:10.1007/s10853-010-4482-8
6. Martin G (1984) Phys Rev B 30:1424
7. Delogu F (2009) Mater Chem Phys 115:641
8. Xi SQ, Zuo KS, Li XG et al (2008) Acta Mater 56:6050
9. Delogu F (2008) Scripta Mater 58:126
10. Jiang WH, Atzmon M (2006) Scripta Mater 54:333
11. Ye J, Liu JW, Enrique RA et al (2003) Scripta Mater 49:969
12. Sheng HW, Lu K, Ma E (1999) J Appl Phys 85:6400
13. Xu J, Collins GS, Peng LSJ et al (1999) Acta Mater 47:1241
14. Ma E, Atzmon M (1995) Mater Chem Phys 39:249
15. Adda Y, Beyeler M, Brebec G (1975) Thin Solid Films 25:107
16. Roussel JM, Bellon P (2002) Phys Rev B 65:144107
17. Wei LC, Averback RS (1997) J Appl Phys 81:613
18. Soisson F, Bellon P, Martin G (1992) Phys Rev B 46:11332
19. Valiev RZ, Estrin Y, Horita Z et al (2006) JOM 4:33
20. Valiev RZ, Langdon TG (2006) Prog Mater Sci 51:881
21. Valiev R, Islamgaliev R, Alexandrov I (2000) Prog Mater Sci 45:103
22. Straumal BB, Kogtenkova OA, Protasova SG et al (2011) J Mater Sci 46:4243. doi:10.1007/s10853-011-5257-6
23. Straumal BB, Baretzky B, Mazilkin AA et al (2004) Acta Mater 52:4469
24. Mazilkin AA, Straumal BB, Rabkin E et al (2006) Acta Mater 54:3933
25. Straumal BB, Mazilkin AA, Protasova SG et al (2009) Mater Sci Eng A 503:185
26. Straumal BB, Dobatkin SV, Rodin AO et al (2011) Adv Eng Mater 13:463
27. Prokoshkin SD, Khmelevskaya IY, Dobatkin SV et al (2005) Acta Mater 53:2703
28. Li W, Li X, Guo G et al (2009) Appl Phys Lett 94:231904
29. Straumal BB, Mazilkin AA, Protasova SG et al (2011) Kovove Mater Metall Mater 49:17
30. Mazilkin AA, Abrosimova GE, Protasova SG et al (2011) J Mater Sci 46:4336. doi:10.1007/s10853-011-5304-3
31. Massalski TB (ed) (1990) Binary alloy phase diagrams. ASM International, Materials Park, OH
32. Coles BR (1955–1956) J Inst Metals 84:346
33. Lihl F, Ebel H, Reichl A et al (1968) Z Metallkunde 59:735
34. Mazilkin AA, Kogtenkova OA, Straumal BB et al (2005) Def Diff Forum 237:739
35. Straumal BB, Mazilkin AA, Protasova SG et al (2008) Acta Mater 56:6246
36. Straumal BB, Baretzky B, Mazilkin AA et al (2009) J Eur Ceram Soc 29:1963
37. Jesser WA, Shneck RZ, Gile WW (2004) Phys Rev B 69:144121

38. Mehrer H (ed) (1990) Diffusion in solid metals and alloys, Landolt-Börnstein New Series, Gr III, vol 26. Springer-Verlag, Berlin
39. Schaeffer H-E (1987) Phys Stat Sol (a) 102:47
40. Straumal BB, Klinger LM, Shvindlerman LS (1984) Acta Metall 32:1355
41. Molodov DA, Straumal BB, Shvindlerman LS (1984) Scripta Metall 18:207
42. Divinski SV, Reglitz G, Rösner H et al (2011) Acta Mater 59:1974
43. Amouyal Y, Divinski SV, Estrin Y et al (2007) Acta Mater 55:5968
44. Bellon P, Averback RS (1995) Phys Rev Lett 74:1819